Supplementary information for "Charge Transport in Azobenzene-Based Single-Molecule Junctions"

Youngsang Kim,[1] Aran Garcia-Lekue,[2] Dmytro Sysoiev,[3] Thomas Frederiksen,[2,4] Ulrich Groth,[3] and Elke Scheer[1]

[1] *Department of Physics, University of Konstanz, 78457 Konstanz, Germany*
[2] *Donostia International Physics Center (DIPC) - UPV/EHU, Paseo Manuel de Lardizabal 4, E-20018 San Sebastian, Spain*
[3] *Department of Chemistry, University of Konstanz, 78457 Konstanz, Germany*
[4] *IKERBASQUE, Basque Foundation for Science, E-48011, Bilbao, Spain*

YK and AGL contributed equally to this work
Corresponding author: ES (elke.scheer@uni-konstanz.de)
Present address: YK (Department of Mechanical Engineering, University of Michigan, Ann Arbor, MI-48109, USA)

Contents

1. SYNTHESIS AND CHARACTERIZATION OF MOLECULES: *ACETYLATED 4,4-BIS(MERCAPTOMETHYL)-AZOBENZENE*

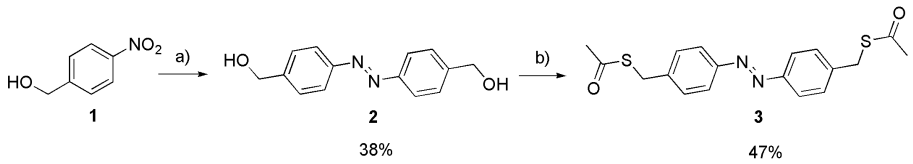

Reagents and conditions: a) NaOH, Zn, ethanol/water, then O_2; b) diisopropyl azodicarboxylate, PPh_3, thioacetic acid, THF, N_2, from 0 °C to RT, 6 h. Product **2** was prepared using the synthetic procedure for 4-hydroxyethyl nitrobenzene described [1]. The absorption spectroscopy of product **3** is presented in Fig. S1.

a) 4-hydroxymethyl nitrobenzene (1) (10 g, 65.3 mmol) was dissolved in 75 ml of ethanol. Sodium hydroxide (2.74 g, 68.5 mmol) was dissolved in 15 ml of water and added to the solution containing **1**. The resulting mixture was brought to reflux and Zn powder (34 g) was added in small portions. After refluxing for 90 min the solution was filtered hot and air was bubbled through the filtrate for 2 hours. The volatiles were removed in vacuo and the resulting orange oil was washed with water and crystallized from ethanol and then again from benzene thus giving 3 g of **2** as an amorphous orange mass in 38% yield. ^{1}H NMR (400 MHz, d6-DMSO): 4.62 (br, 4H; CH_2), 5.38 (br, 2H; OH), 7.55 (d, ^{3}JH-H = 8.3 Hz, 4H; CH), 7.88 ppm (d, ^{3}JH-H = 8.3 Hz, 4H; CH). ^{13}C NMR (100 MHz, d6-DMSO): 62.43 (CH_2), 122.34 (CH), 127.11 (CH), 146.25 (CCH_2), 150.85 ppm (CN).

b) Under an N_2 atmosphere, diisopropyl azodicarboxylate (7.87 ml, 40 mmol) was added dropwise at 0 °C to the solution of triphenylphosphine (9.71 g, 37 mmol) in dry THF (25 ml). After stirring at 0 °C for 30 min, the mixture was treated dropwise with a solution of thioacetic acid (2.68 ml, 38 mmol) and 4,4-bis(hydroxymethyl)-azobenzene (**2**) (3 g, 12.4 mmol) in dry THF (25 ml). The resulting mixture was stirred for another 6 h at RT. The reaction was then quenched with methanol and the volatiles were removed in vacuo. The oily residue was dissolved in chloroform and filtered through a column filled with silica thus giving 2 g of **3** as an amorphous orange solid in 47% yield. ^{1}H NMR (400 MHz, $CDCl_3$): 2.37 (s, 6H; CH_3), 4.18 (s, 4H; CH_2), 7.42 (d, ^{3}JH-H = 8.4 Hz; CH), 7.83 ppm (d, ^{3}JH-H = 8.4 Hz; CH). ^{13}C NMR (100 MHz, $CDCl_3$): 30.47 (CH_3), 33.34 (CH_2), 123.35 (CH), 129.73 (CH), 140.99 (CCH_2), 151.81 (CN), 194.96 ppm (C=O). EI-MS: 358.3 $[M]^+$.

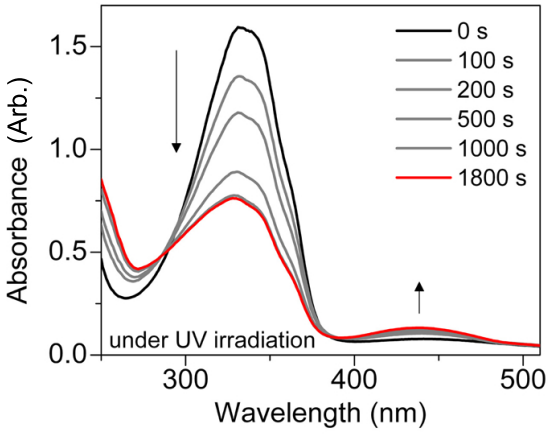

FIG. S1: UV-Visible absorption spectroscopy of Azobenzene-ThioMethyl (AzoTM, species 3) was performed while irradiating UV light with λ=313 nm. The concentration was c = 2.8×10^{-4} mol/l. The photochromic switching from *trans* (black curve) to the photostationary state consisting of 70% *cis* and 30% *trans* (red curve) increases absorption at $\sim$ 440 nm wavelength. The absorption band of the *cis* isomer is at markedly higher wavelength ($\sim$ 440 nm) than the one of the *trans* isomer ($\sim$ 330 nm), suggesting a narrower HOMO-LUMO gap for the *cis* isomer. The thermodynamically favoured ground-state is the *trans* isomer.

Photokinetic measurements: Photokinetic measurements of AzoTM (which contains one CH_2 as a side-group) in Fig. S1 and Azobenzene-ThioEthyl (AzoTE, which contains two CH_2 as a side-group) in Fig. S2 were performed in methanol. UV/Vis spectra were recorded on a Cary 50 spectrometer. The photoirradiation was performed by high-pressure mercury lamp OSRAM HBO 200W/2 in a 1 cm cuvette with a concentration as indicated in the captions of Figs. S1 and S2. The excitation wavelength was isolated by a glass filter centered at 313 nm.

NMR measurements: Azobenzene-ThioEthyl (AzoTE) was preirradiated at 313 nm in deuteromethanol solution until the photostationary state was reached. 1H NMR spectrum of the solution was measured immediately on a Bruker 400 (400 MHz) spectrometer. The *cis*/*trans* ratio in the photostationary state (PSS) was found to be 70%/30%.

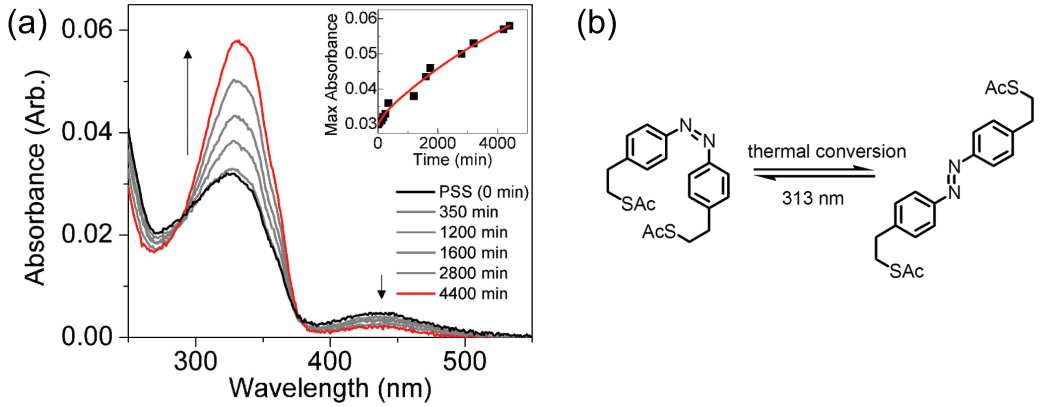

FIG. S2: (a) For probing the thermal stability of the molecules, we measured the thermal back relaxation from the photostationary state (PSS) to the *trans* state at room temperature. For this experiment, we used the electronically equivalent molecule (AzoTE, with two CH_2 groups on each side of the azobenzene moiety) as shown in Fig. S2(b). The concentration was 1×10^{-5} mol/l. We first measured the UV/Vis spectrum in *trans* conformation showing a pronounced maximum at 330 nm with an amplitude of 0.089. We then irradiated the molecules with UV light of $\lambda = 313$ nm until the PSS (black curve) was reached. We then measured the absorption spectrum after the time intervals indicated. The inset shows the value of the maximum absorbance around 330 nm as a function of time. The red line is an exponential fit to the data with a time constant of $\tau = 6500$ min. From these data we estimate that only a few percent of the molecules would have been relaxed back to the *trans* form within the first seven hours after irradiation before they are cooled down to 4.2 K.

2. DEVICE FABRICATION

On the polished bronze wafer (200 μm in thickness), a layer of polyimide (2 μm) is spin-coated. This layer serves as an electrical insulator and a sacrificial layer in the subsequent etching process. On top of the polyimide, a double layer of electron-beam resists (ER), MMA-MAA/PMMA, is deposited by spin-coating (maximum 5000 rpm). Then an electron beam lithography (EBL) process is performed on the prepared wafer. After developing the resin, gold of about 80 nm thickness is deposited using electron beam evaporation at a pressure of about 10^{-8} mbar. Finally, dry etching with O_2 plasma in a reactive ion etcher (RIE) is performed in order to form a free-standing bridge [2, 3]. The SEM image of a finalized sample is presented in Fig. S3(a). The schematics of metal-molecule-metal junctions for *trans* and *cis* forms is also displayed in Fig. S3(b). A dilute solution of molecules ($\sim10^{-4}$ M) in 5 ml ethanol is prepared, and then the *trans* or the *cis* isomers are initialized by irradiating visible or UV light during about 24 hours, respectively. The samples are immersed in the molecular solution for $\sim$5 hours in the dark. To remove the acetyl ($COCH_3$, denoted as Ac) groups, a droplet of ammonium hydroxide (NH_4OH) is added [4, 5]. After the incubation time the remaining molecular solution is rinsed off in ethanol and the sample is blown dry by nitrogen gas. As described above, after irradiation with visible light 100% of the molecules are in the *trans* conformation. In the photostationary state after

UV illumination 70% of the molecules are in their *cis* conformation. The azobenzene-based molecules undergo a thermal transformation of the *cis* form to the *trans* form. However, the relaxation time depends on the temperature and the electronic properties of the substituents. The introduction of the electron-donating groups with positive mesomeric effect such as thiomethyl (SCH_3) results in an increased rate of *cis* to *trans* conversion of the azobenzene molecule [6]. In our molecules this potentially "destabilizing" thiomethyl group is separated by the CH_2-joint-like unit which acts as an isolator. Moreover, the *cis* to *trans* transformation of azobenzenes is temperature-dependent [7], and the thermal isomerization rate of this process is proportional to the temperature in thin films and in solution. A change from 314 K to 293 K results in a tenfold lower isomerization rate. This experiment was held at distinctly lower temperatures (4.2 K). We measured the thermal isomerization rate of electronically equivalent derivates with two CH_2-groups on each side of the azobenzene kernel at room temperature in methanol and found a decay time of > 100h, see Fig. S2. Therefore, the isomerization is expected to be negligible during the measurement process as well as during the sample preparation.

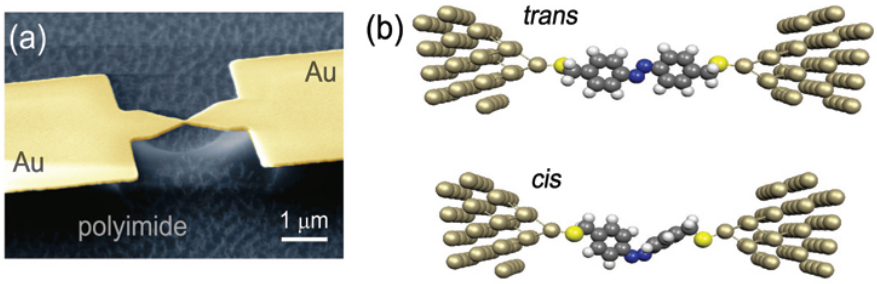

FIG. S3: (a) A representative SEM image of MCBJ sample. (b) Schematics of metal-molecule-metal junctions for *trans* and *cis* isomers. For the DFT calculation these structures were used.

3. CONDUCTANCE HISTOGRAMS

The conductance histogram in Fig. S4 was built using the conductance curves obtained while opening and closing junctions (about 700 times each) at low temperature. The conductance has been measured with a linear amplifier and thus a linear binning of width $5\times10^{-8}G_0$ has been used for calculating the histogram. The *cis* isomers show a conductance around three times higher than the *trans* isomers. The conductance of both isomers is very closer to the noise level, in the order of $10^{-7}G_0$. The absence of a peak in the histogram of the *cis* conformation at the preferred conductance value of the *trans* isomer ($1.6\times10^{-7}G_0$) is an additional indication that the thermal isomerization from *cis* to *trans* is negligible. The appearance of a higher peak in the *trans* histogram around $3.3\times10^{-7}G_0$, i.e. twice the preferred conductance of the *trans* single-molecule conductance may indicate the formation of larger than single-molecule junctions. In the study by Martin *et al.* [8] dibenzoic molecules, very similar to azobenze molecules, were investigated using a STM. In that case, single molecule junctions without CH_2 side-chains were formed and conductances of the order of $10^{-5}G_0$ were reported for *trans* isomers. Mativetsky *et al.* [9] reported conductances of azobenzene molecules containining four fully conjugated phenyl rings to be in the order of $10^{-5}G_0$. This value was achieved using C-AFM with a tip area of 25 nm^2, which is expected to contain more than 1000 molecules. Therefore, a single molecule could show conductances in the range of $10^{-8}G_0$. Our AzoATM molecules are not conjugated resulting in rather low conductance (more than 2 orders of magnitude decrease are expected due to the saturated CH_2 side-chains) than the usual azobenzene molecules. One could consider the possibility of one-side of the molecule being detached from the metal electrode, which would significantly reduce the conductance. However, in our measurements, we clearly see the single-molecule conductance plateau, as well as antisymmetric I-Vs and IETS. Moreover, we observe the vibrational mode at about 25mV, originating from Au-S stretching modes (see Fig. S7). These results support our conclusion that the measured low conductances are true values obtained from single Au-AzoATM-Au molecular junctions.

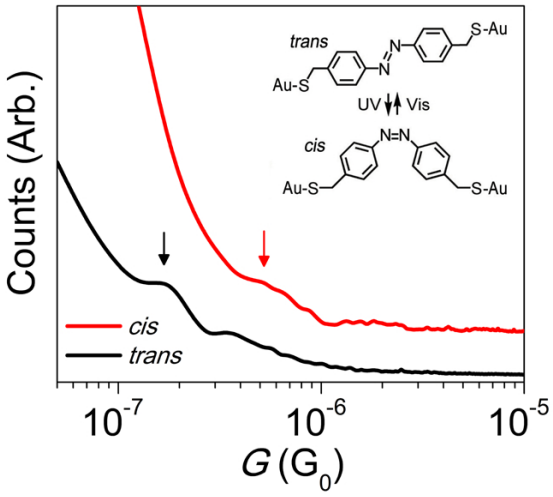

FIG. S4: The conductance histograms of the molecular junctions are presented for *trans* (black) and *cis* (red) isomers, respectively, after repeating the breaking and closing process about 700 times for each isomer. The arrows indicate the prominent conductance peak of the histograms at the lowest conductance regime. By fitting a Lorentzian function to the data, the preferred conductance value is obtained $(1.6\pm0.7)\times10^{-7}$G$_0$ and $(4.9\pm3.4)\times10^{-7}$G$_0$ for *trans* and *cis*, respectively.

4. TEMPERATURE-VARIABLE CURRENT-VOLTAGE (I-V) MEASUREMENTS

The temperature-variable I-V curves for Au-AzoATM-Au junction are obtained between 4.2 and 40 K as shown in Fig. S5. A temperature dependence of the current via a single molecule is not observed, which indicates that coherent off-resonant tunneling is the charge conduction mechanism for these junctions.

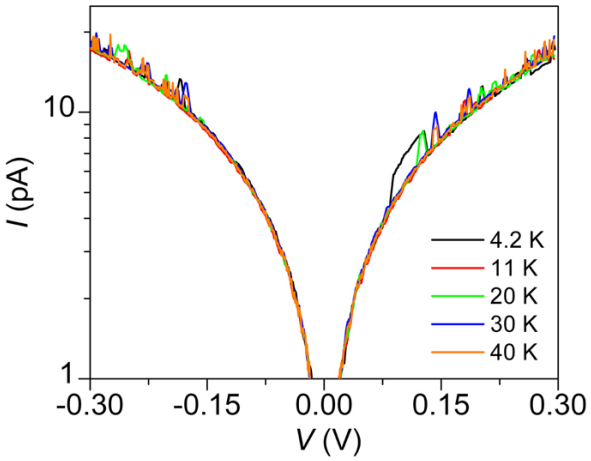

FIG. S5: Temperature independent I-V curves for a *trans* isomer between 4.2 K and 40 K.

5. INELASTIC ELECTRON TUNNELING SPECTROSCOPY (IETS)

As presented in Fig. 3(a) of the manuscript, the averaged IETS measured at the lowest conductance regime ($\sim 10^{-7}$G$_0$) displays negative d^2I/dV^2 values at positive bias regime. The experimentally measured IETS (d^2I/dV^2) are presented without the normalization by dI/dV owing to the low value of conductance. The averaged curves shown in Fig. 3 were obtained from five individual curves recorded in different junction situations shown in Fig. S6. In order to compare the experimentally obtained IETS, we average several IETS spectra in different junction situations. We compare the averaged curve with theoretically obtained averaged IETS. The amplitude of the positive peaks is only slightly bigger than the negative contributions, meaning that the mean signal is close to zero. This negative baseline may be indicative of at least three independent situations. 1: The overall curvature of the underlying I-V is negative. 2: The signal is not caused by inelastic excitations but dominated by noise or other effects. 3. A negative offset of the lock-in amplifier measuring the second derivative. Case 1 can be clearly excluded because the I-Vs are well described by the single-level model that displays I-Vs with positive curvature in the off-resonant situation probed here. In the following, we argue why also case 2 can be ruled out. The five IETS spectra in Fig. S6 are indeed antisymmetric as shown in Fig. S7, and as expected for signals originating from inelastic excitations [10]. In addition, as presented in Fig. S7(a), the IETS measured at higher conductance regime ($\sim 10^{-5}$G$_0$) shows well pronounced antisymmetric curves respect to the zero bias, i.e. positive values at positive bias and negative values at negative bias regime. Furthermore, the vibrational energies of IETS in high (Fig. S7(a)) and low (Fig. S7(b)) conductance regimes appear at similar bias regime (especially between 150mV and 220mV for both polarities). These comparisons support that the IETS spectra measured below 10^{-6}G$_0$ show the true vibrational excitations. Hence, we argue that the d^2I/dV^2 signals are suppressed because of a drift of the offset voltage of the lock-in amplifier during the recording of the IETS. The low signal to noise ratio in this low conductance regime implies long integration times of up to $\sim$8 minutes per trace.

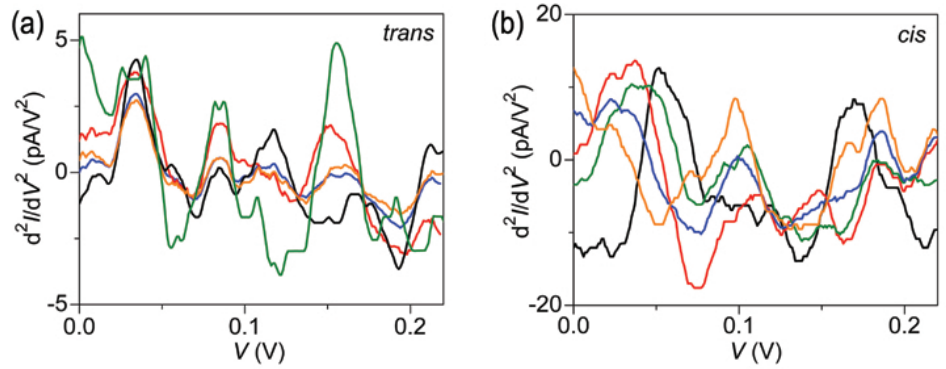

FIG. S6: The different curves of five IETS were measured at molecular conductance plateau for (a) *trans* and (b) *cis* isomers. These curves were averaged and presented in Fig. 3(a) of the manuscript.

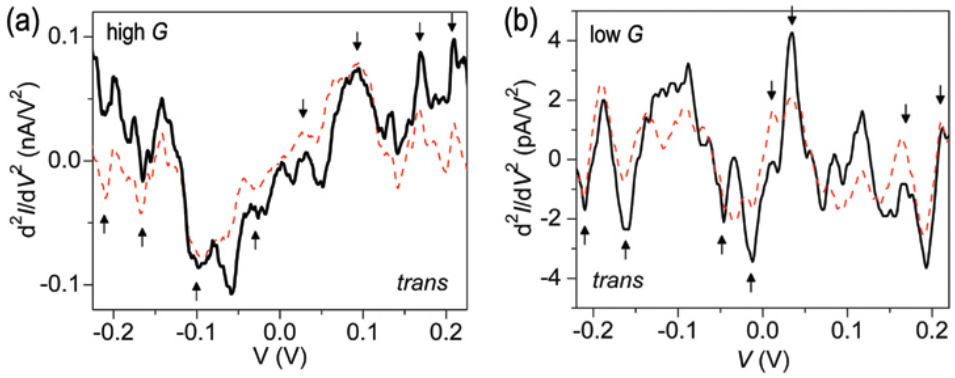

FIG. S7: A representative IETS spectrum (black) measured at (a) high conductance regime and (b) low conductance regime of *trans* isomer is shown together with a curve antisymmetrized (red) with respect to the bias polarity, obtained by the simple formula $y = (f(x) - f(-x))/2$. The similarity (especially position of peaks between 150mV and 220mV) of both traces implies that the peaks correspond to excitations of the molecular junction. Arrows indicate vibrational excitations which appear symmetrically for positive and negative biases.

6. ELECTRON TRANSPORT MODELS

To deduce a microscopic understanding of the charge transport through single organic molecules we consider the following models.

A. Single-Level Model

The single-level model assumes the current to be carried by a single molecular orbital (MO) at the energy E_0 from the Fermi energy E_F, symmetrically coupled via the coupling constants Γ to right and left leads [as schematically shown in Fig. S8(a)]. The coupling results in a broadening of the level and yields a resonance with Lorentzian shape for the transmission function [2, 11, 12]

$$T(E) = \frac{\Gamma^2}{(E - E_0)^2 + \Gamma^2}. \tag{1}$$

The current is calculated according to the Landauer formula as an integration over the bias window

$$I(V) = \frac{2e}{h} \int_{-\infty}^{\infty} T(E) \left[f(E - eV/2) - f(E + eV/2) \right] dE, \tag{2}$$

where e is the electron charge, h Planck's constant, and $f(E)$ the Fermi-Dirac distribution function. In the symmetric coupling case the energy level E_0, and thus $T(E)$, are assumed to be independent of the voltage.

Each experimental $I - V$ curve was fitted with this model and the level alignment E_0 and the level broadening Γ were inferred from these fits. The zero-bias conductance is given by $G = \mathrm{G}_0 T(E_F)$.

B. Fano-Resonance Model

The Fano-resonance model assumes two energy levels, E_0 and E_1 (as measured from E_F), with a weak coupling t between the sites. The molecular orbital with energy E_0 is symmetrically coupled to left and right electrodes via the coupling constant Γ. The molecular orbital of energy E_1 is strongly localized in the molecular region and thus one can consider it to be uncoupled from the electrodes. Within this scenario, schematically depicted in Fig. S8(b) the transmission can be expressed as [11]

$$T(E) = \frac{\Gamma^2}{\left[E - E_0 - t^2/(E - E_1) \right]^2 + \Gamma^2} \tag{3}$$

and the corresponding current can be obtained by substituting Eq. (3) in the Landauer formula of Eq. (2). The zero-bias conductance is then, as for the single-level model, given by $G = \mathrm{G}_0 T(E_F)$.

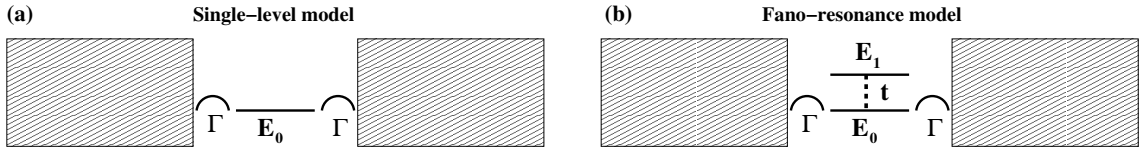

FIG. S8: Schematic diagrams of (a) single-level and (b) Fano-resonance transport models.

7. FIRST-PRINCIPLES SIMULATIONS

A. Computational details

The SIESTA calculations were done using the generalized gradient approximation for exchange-correlation [13] and a cutoff of 300 Ry for the real-space grid integrations. The basis set consisted of single-zeta plus polarization orbitals for Au atoms and split-valence double-zeta plus polarization orbitals for C, N, H and S atoms. Atomic coordinates of the azobenzene molecule, tip, and surface gold atoms were relaxed until forces were smaller than 0.02 eV/Å. During geometry optimization, phonon calculations, and for the TRANSIESTA calculations a Monkhorst-Pack mesh with $2 \times 2 \times 1$ k-point sampling of the three-dimensional Brillouin zone was used. The transmission functions were sampled over 10×10 k-points and the IETS spectra calculated at the Γ-point using the INELASTICA code [14].

B. Azobenze molecular orbitals

With the aim of being able to identify the main character of the resonant levels which dominate the charge transport in *cis*/*trans* azobenzene-based junctions, we have first investigated the gas-phase azobenzene molecules. The lowest unoccupied molecular orbital (LUMO), the highest occupied molecular orbital (HOMO) and the HOMO-1 orbital for the gas-phase *cistrans* isomers are represented in Fig. S9, together with a schematic energy diagram of the molecular orbitals with respect to their corresponding Fermi level. We observe that the energy separation between the HOMO and HOMO-1 levels is much smaller for the *trans* isomer. Besides, whereas the HOMO-1 level of the *trans* is extended over the whole molecule, its HOMO of is strongly localized in the region of the N=N bond. In the *cis* case, all the molecular orbitals lying close to the Fermi level extend over the entire molecular region.

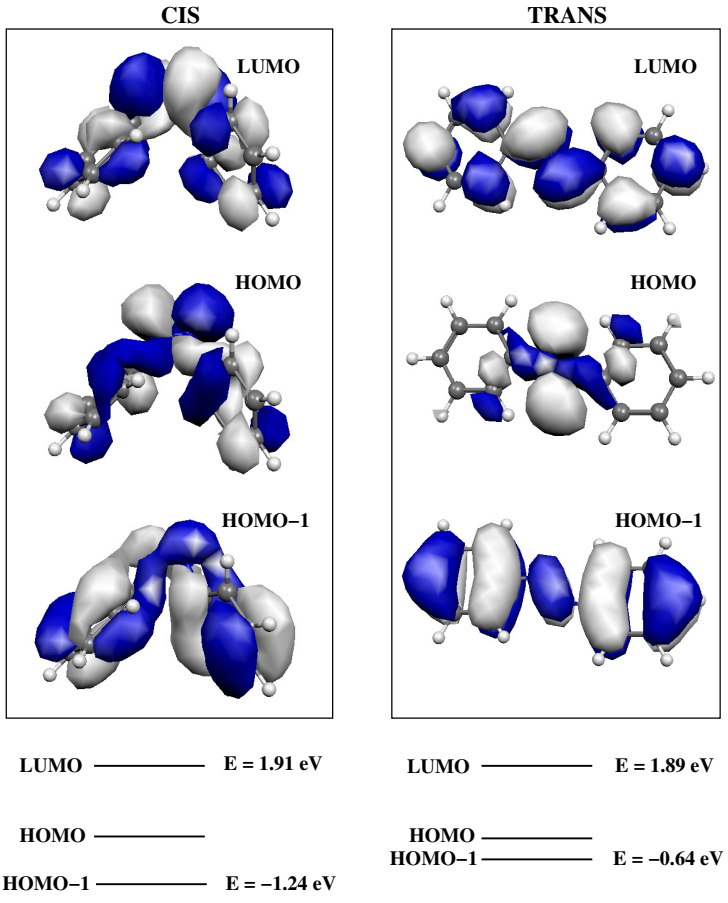

FIG. S9: LUMO, HOMO and HOMO-1 orbitals of *cis* (left) and *trans* (right) azobenzene molecules, respectively, together with their corresponding energy level diagrams. The energy values are measured with respect to the HOMO level of each isomer.

C. Transmission fitting

In Fig. S10 we have represented the calculated transmission curves for *cis*/*trans* isomers for a chosen electrode-electrode separation (solid lines), together with the corresponding fitted curves (dashed lines).

As shown in Fig. S10(a), in the *cis* case the transmission at the Fermi energy is dominated by the tail of the peak at ~ -0.1 eV. The corresponding dominant transmission eigenchannel [see right side of Fig. S10(a)] is extended across the whole molecule and resembles the gas-phase HOMO molecular orbital of *cis* azobenzene represented in Fig. S9. Hence, the transport at E_F in *cis* AzoATM junctions can then be fitted using the single-level model described above, with fitting parameters $E_0 = -0.089$ eV and $\Gamma = 0.005$ eV.

For the *trans* isomers, we observe a double-peak feature in the transmission, as can be seen in Fig. S10(b). The transmission eigenchannels dominant at the energy of each of the peaks are shown as well [see right side of Fig. S10(b)], and from the comparison to the molecular orbitals of gas-phase *trans* azobenzene in Fig. S9 we can identify them as related to gas-phase HOMO-1 and HOMO molecular orbitals, respectively. These two dominant transmission eigenchannels for *trans* isomers, lie close in energy and their interference gives rise to the double-peak feature, which contains a wide peak and a Fano-like resonance [11]. The latter has its origin in a molecular orbital strongly localized in the N=N bond region and thus it has a negligible contribution to the conductance at the Fermi level. Consequently, the transmission at E_F may be mainly attributed to the delocalized level. This scenario can be adequately described by the Fano-resonance model introduced above and, accordingly, a nice fitting of the transmission curve of Fig. S10(b) to this model is achieved. The corresponding fitting parameters are $E_0 = -0.172$ eV, $E_1 = -0.121$ eV, $\Gamma = 0.004$ eV and $t = 0.015$ eV.

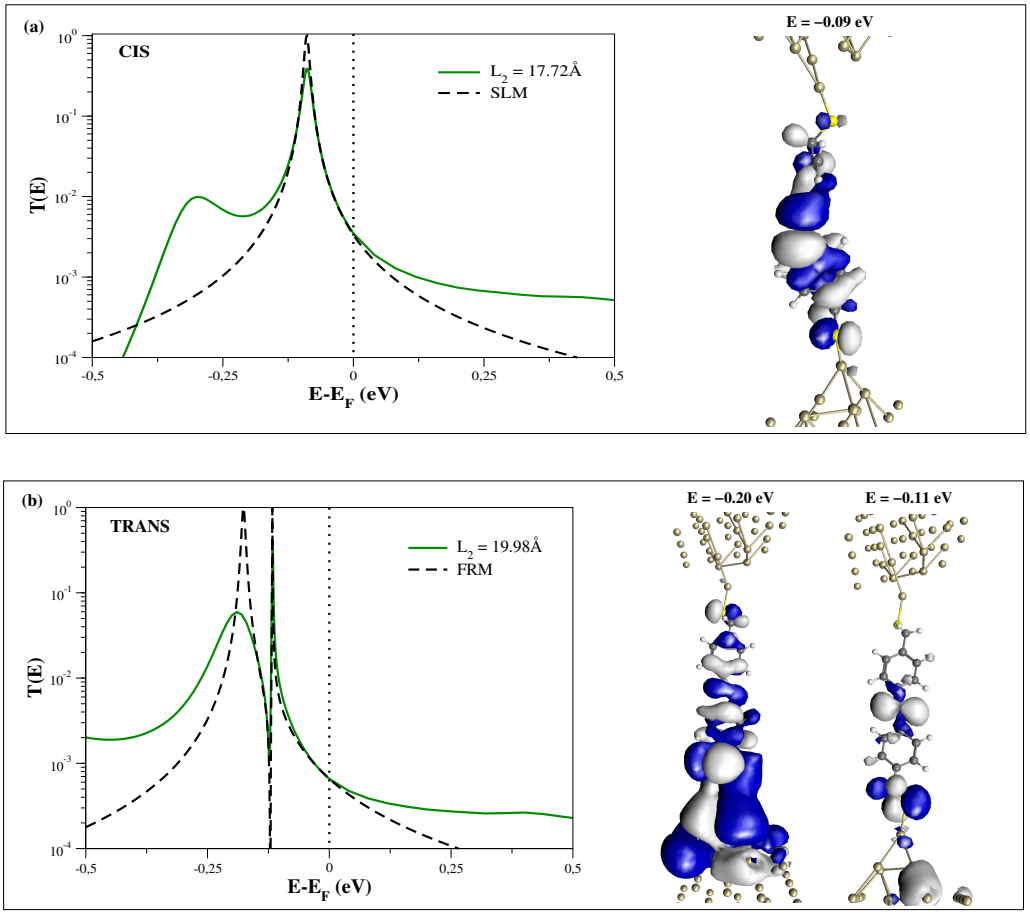

FIG. S10: Transmission curves for (a) *cis* and (b) *trans* Au-AzoATM-Au,respectively, for a chosen electrode-electrode separation. The dashed lines in (a) and (b) indicate the single-level and Fano-resonance model fits. The corresponding dominant eigenchannels incoming from the bottom side for each isomer are shown on the right side of (a) and (b) for *cis* and (b) *trans*, respectively.

D. IETS spectra

Figure S11 shows the IETS spectra for *cis* and *trans* isomers at three different stretching conditions, together with the corresponding averaged spectra (solid curves). The IETS spectra have been antisymmetrized following the procedure described in the caption to Fig. S7. L denotes the electrode separation between the Au atoms binding to the molecule. The initial electrode separations are of the order of those previously used for similar junctions [15], as the actual experimental values are not known. As observed in Fig. S11, IETS spectra for *cis*/*trans* forms are significantly different, specially in the high-energy regime.

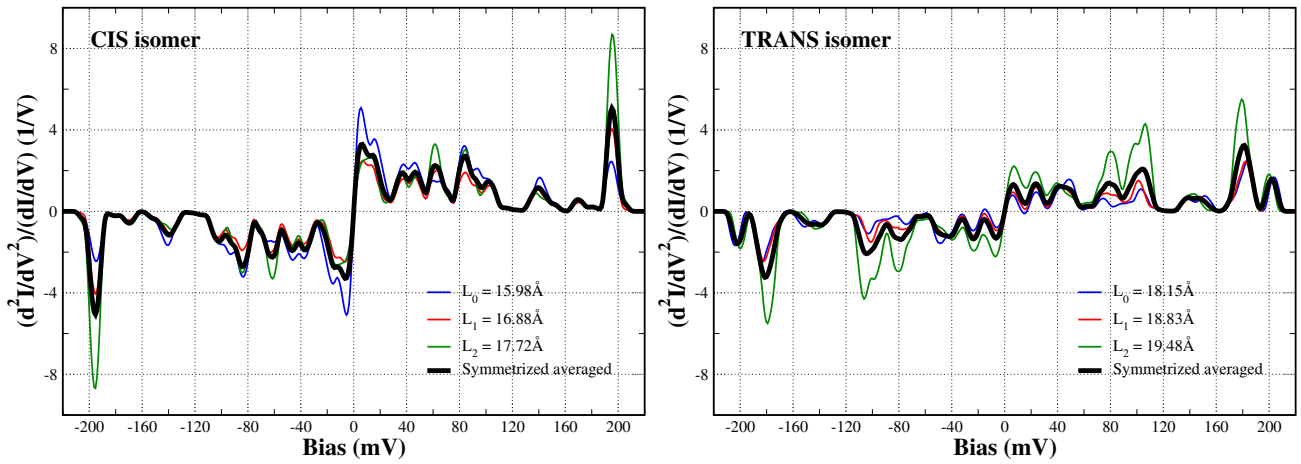

FIG. S11: Simulated IETS spectra of *cis* (left) and *trans* (right) Au-AzoATM-Au, respectively, for three different stretching conditions. The thick solid lines represent the antisymmetrized, averaged IETS spectra. The length L is measured between the Au apex atoms.

In order to extract information about the vibration modes responsible for the distinctive IETS signals in the 120-200 mV range of Fig. S8, we have calculated the projection P_i^λ of each vibration mode λ of the system onto different characteristic modes i, defined as follows:

$$0 \leq P_i^\lambda = \frac{\mathbf{v}_\lambda \cdot \mathbf{v_i}}{|\mathbf{v}_\lambda||\mathbf{v_i}|} \leq 1, \tag{4}$$

where $\mathbf{v}_\lambda$ is the eigenvector of mode λ of the *cis*/*trans* isomers. The vector $\mathbf{v}_i$ represents a particular *probe mode* such as shown in the lower panel of Fig. S12, which in essence measures the extent of N=N stretching ($i = 1$), C-N out-of-phase stretching ($i = 2$), C-N in-phase stretching ($i = 3$), C-C symmetric stretching ($i = 4$), C-C antisymmetric stretching ($i = 5$). Hence, for each vibration mode v_λ, the values of P_i^λ measure to what extent mode λ carries the character of probe mode i. By performing this analysis for all the vibration modes of our *cis*/*trans* isomers, we can learn about the character of the vibration modes dominant in the IETS spectra of both molecular isomers.

The change in conductance $\Delta\sigma_\lambda \equiv \Delta\,(dI/dV)_\lambda$ for each vibration mode λ can – within the lowest order expansion (LOE) approach considered here and neglecting asymmetric contributions to the inelastic current – be expressed as [16, 17]

$$\Delta\sigma_\lambda = \mathrm{Tr}\left[\mathbf{G}^\dagger\mathbf{\Gamma}_L\mathbf{G}\left\{\mathbf{M}_\lambda\mathbf{G}\mathbf{\Gamma}_R\mathbf{G}^\dagger\mathbf{M}_\lambda + \frac{i}{2}\left(\mathbf{\Gamma}_R\mathbf{G}^\dagger\mathbf{M}_\lambda\mathbf{A}\mathbf{M}_\lambda - \mathrm{H.c.}\right)\right\}\right], \tag{5}$$

where $\mathbf{G}$, $\mathbf{A}$ and $\mathbf{\Gamma}_{L,R}$ represent the retarded Green's function, the spectral function defined as $\mathbf{A} = i(\mathbf{G} - \mathbf{G}^\dagger)$, and the electrode couplings, respectively. The electron-vibration coupling matrix for mode λ is denoted $\mathbf{M}_\lambda$. In the LOE scheme, all these quantities are evaluated at the Fermi energy.

The combined analysis of mode character and IETS weight is summarized in the upper panels of Fig. S12, where we have represented P_i^λ as a function of the mode energy $\hbar\omega$ for *cis* (left panel) and *trans* (right panel) isomers.

The color code allows the identification of the contributions corresponding to each of the probe modes shown in the lower panel of Fig. S12. The area of each data point is proportional to the change in conductance given by Eq. (5), so that large points allow us to identify visually the vibration modes giving a strong contribution to the IETS spectrum. For comparison we have included the corresponding IETS curves (solid lines). Taking into account all the information included in Fig. S12, we can thus conclude that both for *cis* and *trans* isomers the main peaks in the IETS are originated by modes with a strong N=N stretching component ($i = 1$), together with a smaller in-phase C-N stretching ($i = 3$) contribution.

In Tab. I, we present the numerical values of P_i^λ for the dominant vibration modes of *cis* and *trans* isomers at a chosen stretching condition. For *cis* case, the IETS spectrum is dominated by a peak at ~ 195 meV which, as observed from Tab. I, is originated by two vibration modes of dominant N=N stretching character ($i = 1$). Both modes, specially the one at 196 meV, have also a strong contribution from the C-N in-phase stretching ($i = 3$). For the *trans* isomer, the largest IETS peak is also originated by two modes with a dominant N=N stretching character ($i = 1$). The mode at 178 meV exhibits as well a significant contribution from the C-N out-of-phase stretching ($i = 2$). The corresponding IETS curves have dominant IETS signals at ~ 196 meV and ~ 179 meV, that is, peaks separated by ~ 20 meV, in fair agreement with experimental IETS measurements. The same conclusion is obtained by performing this mode analyis at different stretching conditions.

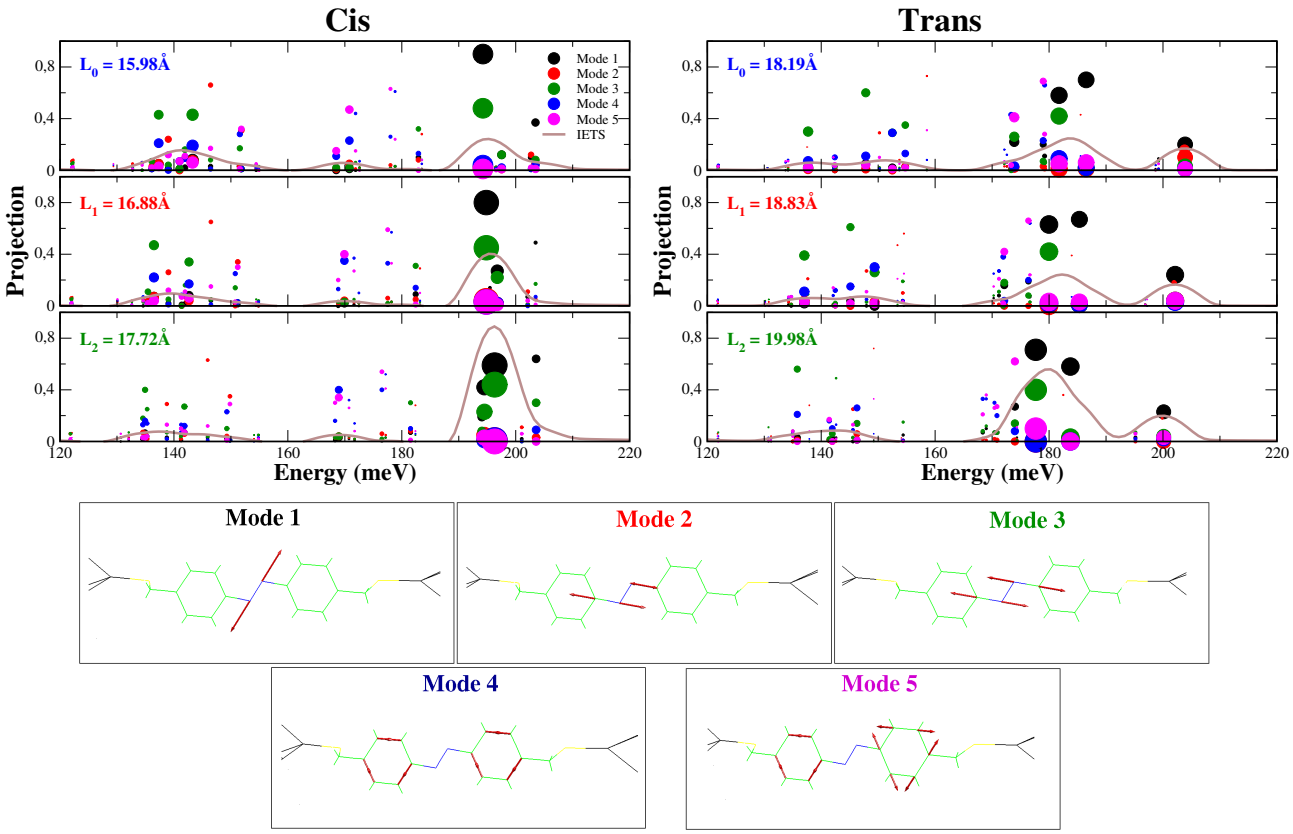

FIG. S12: Projection of the vibration modes of *cis* and *trans* isomers onto the characteristic modes depicted in the lower panels. The area of the points is proportional to the change in conductance. IETS spectra are represented with solid lines. The length L is measured between the Au apex atoms.

TABLE I: Vibration energy $\hbar\omega$ (in meV) and projection P_i^λ of the dominant vibration modes onto the probe modes shown in the lower panel of Fig. S12, for *cis* and *trans* isomers at L_2 stretching condition.

cis

$\hbar\omega$ (meV)	N=N stretch ($i=1$)	C-N out-of-phase stretch ($i=2$)	C-N in-phase stretch ($i=3$)	C-C symm. stretch ($i=4$)	C-C antisymm. stretch ($i=5$).
196	0.62	0.01	0.45	0.01	0.01
195	0.37	0.04	0.19	0.01	0.03

trans

$\hbar\omega$ (meV)	N=N stretch ($i=1$)	C-N out-of-phase stretch ($i=2$)	C-N in-phase stretch ($i=3$)	C-C symm. stretch ($i=4$)	C-C antisymm. stretch ($i=5$).
184	0.57	0.03	0.01	0.00	0.01
178	0.72	0.41	0.00	0.00	0.10

E. Projected density of states

In Fig. S13 we have represented the projected density of states (PDOS) for the same *cis* and *trans* isomers, as obtained using a $20 \times 20 \times 1$ k-point sampling and a broadening of 50 meV. For *trans* isomers, we observe that the PDOS near Fermi level (E_F) is dominated by states in the occupied side and with a strong N contribution. For *cis* isomers, occupied states with strong N and C contributions dominate the PDOS at the Fermi level. Besides, both for *cis* and *trans* forms, the contribution from S atoms is also significant at energy values slightly lower but still close to the Fermi level. Most importantly, at all stretching conditions the peaks of the PDOS are closer to E_F in the *cis* than in the *trans* isomer, which is reflected in the corresponding transmission curves (Fig. 2 of the manuscript).

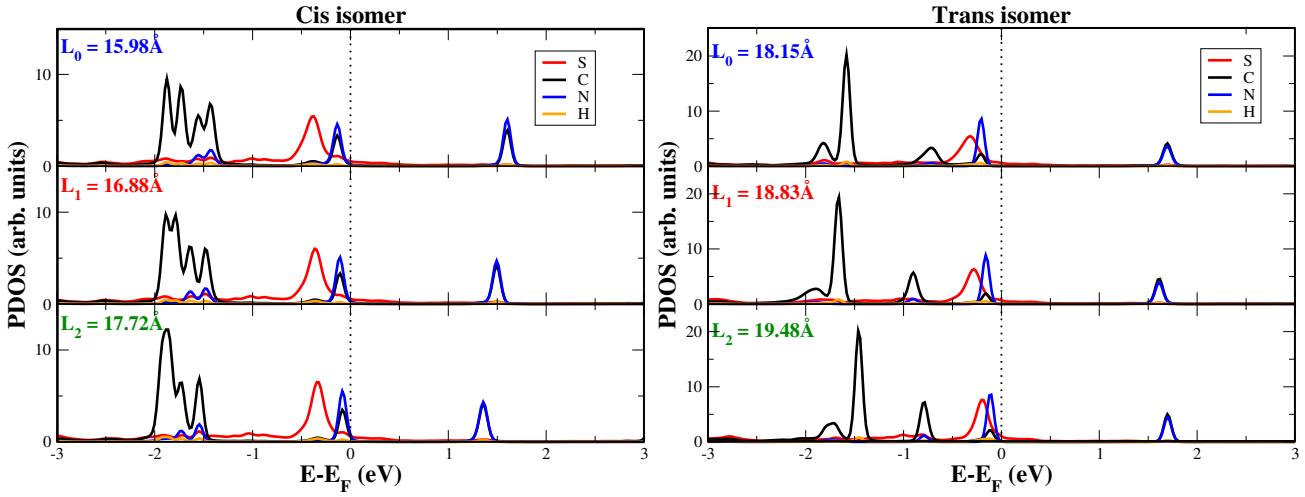

FIG. S13: Simulated projected density of states (PDOS) for *cis* (left panels) and *trans* (right panels) Au-AzoATM-Au junctions at three different stretching conditions. The length L is measured between the Au apex atoms.

F. Transmission eigenchannels

The scattering states corresponding to the most transmitting eigenchannel (incoming from the right) for *cis* (left) and *trans* (right) isomers are visualized in Fig. S14 for each of the three considered stretching conditions [18]. In all cases, the eigenchannel for the *cis* isomer reaches further into the junction as compared to the *trans* form (for the same isosurface value). Consequently, the transmission is always larger for the *cis* isomer. Besides, the decay length of the *cis* eigenchannel is not significantly affected by the stretching and, hence, the conductance at Fermi level does not change much when the electrode separation is increased. For the *trans* case on the other hand, the decay length of the eigenchannel decreases considerably as the junction is stretched, giving rise to a marked decrease of the Fermi level conductance. These findings are of course in agreement with the results reported in Fig. 2 of the manuscript.

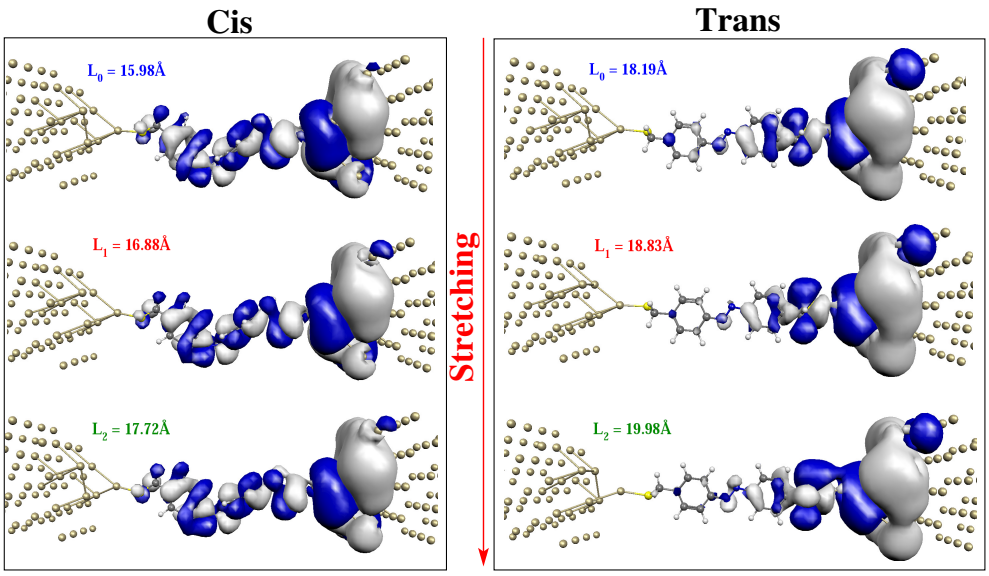

FIG. S14: Isosurface plots of the most transmitting eigenchannel for *cis* (left panels) and *trans* (right panels) Au-AzoATM-Au junctions at three different stretching conditions.

[1] P. Ahonen, T. Laaksonen, D. J. Schiffrin, and K. Kontturi, Phys. Chem. Chem. Phys. **9**, 4898 (2007).
[2] Y. Kim, T. Pietsch, A. Erbe, W. Belzig, and E. Scheer, Nano Lett. **11**, 3734 (2011).
[3] Y. Kim, T. J. Hellmuth, M. Bürkle, F. Pauly, and E. Scheer, ACS Nano **5**, 4104 (2011).
[4] H. Valkenier, E. H. Huisman, P. A. van Hal, D. M. de Leeuw, R. C. Chiechi, and J. C. Hummelen, J. Am. Chem. Soc **133**, 4930 (2011).
[5] M. T. González, E. Leary, R. García, P. Verma, M. A. Herranz, G. Rubio-Bollinger, N. Martín, and N. Agraït, J. Phys. Chem. C **115**, 17973 (2011).
[6] H. Nichioka, T. Kato, and H. Asanuma, Angew. Chem. Int. **51**, 1165 (2012).
[7] Z. F. Liu, K. Morigaki, T. Enomoto, K. Hashimoto, and A. Kujishima, J. Phys. Chem. **96**, 1875 (1992).
[8] S. Martin, W. Haiss, S. J. Higgins, and R. J. Nichols, Nano Lett. **10**, 2019 (2010).
[9] J. M. Mativetsky, G. Pace, M. Elbing, M. A. Rampi, M. Mayor, and P. Samori, J. Am. Chem. Soc **130**, 9192 (2008).
[10] T. Böhler, A. Edtbauer, and E. Scheer, Phys. Rev. B **76**, 125432 (2007).
[11] J. C. Cuevas and E. Scheer, *Molecular Electronics: An Introduction to Theory and Experiment* (World Scientific Publishers, 2010), 1st ed.
[12] L. A. Zotti, T. Kirchner, J. Cuevas, F. Pauly, T. Huhn, E. Scheer, and A. Erbe, Small **6**, 1529 (2010).
[13] J. P. Perdew, K. Burke, and M. Ernzerhof, Phys. Rev. Lett. **77**, 3865 (1996).
[14] `http://inelastica.sourceforge.net/`.
[15] C. Zhang, M.-H. Du, H.-P. Cheng, X.-G. Zhang, A. E. Roitberg, and J. L. Krause, Phys. Rev. Lett. **92**, 150301 (2004).
[16] M. Paulsson, T. Frederiksen, and M. Brandbyge, Phys. Rev. B **72**, 201101 (2005).
[17] T. Frederiksen, M. Paulsson, M. Brandbyge, and A.-P. Jauho, Phys. Rev. B **75**, 205413 (2007).
[18] M. Paulsson and M. Brandbyge, Phys. Rev. B **76**, 115117 (2007).